Th A4 11

Interpretational Aspects of Multispectral Coherence

K.J. Marfurt* (University of Oklahoma)

Summary

Seismic coherence volumes are routinely used to delineate geologic features that might otherwise be overlooked on conventional amplitude volumes. In general, the quality of a coherence image is a direct function of the quality of the input seismic amplitude data. However, even after careful processing, certain spectral components will better illuminate a given feature than others. For this reason, one may wish to not only examine coherence computed from different filter banks, but somehow combine them into a single composite image. I do so by summing structure-oriented covariance matrices computed from spectral voices prior to computing coherence. I show that multispectral coherence images are superior to traditional broadband coherence images, even if the seismic amplitude data have been previously spectrally balanced. While much of this improvement can also be found in RGB blended volumes, multispectral coherence provides several advantages: (1) one can combine the information content of more than three coherence volumes, (2) there is only one rather than three volumes to be loaded into the workstation, and (3) the resulting grey-scale images can be co-rendered with other attributes of interest plotted against a polychromatic colour bar, such as P-impedance vs. Poisson's ratio or SOM cluster results.

Introduction

Twenty years after its inception in the mid-1990s, seismic coherence volumes are routinely used to delineate faults and stratigraphic edges, to highlight incoherent zones such as karst collapse and mass transport complexes, and to identify subtle tectonic and sedimentary features that might otherwise be overlooked on conventional amplitude volumes. In general, the quality of a coherence image is a direct function of the quality of the seismic amplitude from which it is computed. For this reason, the most important step in coherence computation is to ensure that the processor provides data that exhibit high bandwidth, are accurately imaged, and are free of multiples and other types of coherent noise. Once in the interpreter's hands, many seismic amplitude volumes benefit from subsequent post-stack structure-oriented filtering and spectral balancing (Chopra and Marfurt, 2007). In spite of this effort, certain spectral components will exhibit a higher signal-to-noise ratio than others. In addition, thin beds that are tuned might be expected to better exhibit discontinuities at their higher amplitude tuning frequency than at other frequencies. For this reason, one may wish to not only examine coherence computed from different filter banks, but somehow combine them into a single composite image.

Method

The covariance matrix and energy ratio coherence

Gersztenkorn and Marfurt (1999) describe the first implementation of coherence based on eigenvectors of the covariance matrix. Since that time, several details have been modified, including computing the covariance matrix, **C**, from the analytic trace, composed of the original data, **d**, and its Hilbert transform, $\mathbf{d^H}$ along structural dip:

$$C_{mn} = \sum_{k=-K}^{K} \left[d(t_k, x_m, y_m) d(t_k, x_n, y_n) + d^H(t_k, x_m, y_m) d^H(t_k, x_n, y_n) \right] \quad (1)$$

where t_k is the time of a structurally interpolated sample at a distance (x_m,y_m) about the analysis point at $(x=0, y=0,t=0)$. In the examples shown later, K=5 samples, and n=1,2,..M, m=1,2,..,M where M=5 traces, centred about the analysis point. Computing the eigenvectors of **C** provides a means of computing a Karhunen-Loève filtered version of the data, $\mathbf{d_{KL}}$ and $\mathbf{d^H_{KL}}$. If the data **d** have been previously spectrally balanced, the broadband energy ratio coherence (Chopra and Marfurt, 2007), s_{bb}, can then be defined as

$$s_{bb} = \frac{\sum_{m=1}^{M} \sum_{k=-K}^{K} \left\{ \left[d_{KL}(t_k, x_m, y_m) \right]^2 + \left[d^H_{KL}(t_k, x_m, y_m) \right]^2 \right\}}{\sum_{m=1}^{M} \sum_{k=-K}^{K} \left\{ \left[d(t_k, x_m, y_m) \right]^2 + \left[d^H(t_k, x_m, y_m) \right]^2 \right\}}. \quad (2)$$

Filter banks and spectral decomposition

Hardage (2009) recognized that because of the variable signal-to-noise ratio at different frequencies, that faults were more easily identified in his data on the low frequency components that were less contaminated by strong interbed multiples. Gao (2013) showed how different components of narrow band spectral probes highlighted different edges at different frequencies. The continuous wavelet transform can be viewed as the application of a suite of filter banks to the original seismic data. Li and Lu (2014) and Honorio et al. (2016) computed coherence from a suite of spectral components and combined them using RGB colour blending, resulting in not only improved discontinuity images, but in addition an estimate at which spectral bands the discontinuities occurred. The main limitation of this approach is that only three spectral components can be co-rendered at any one time.

To address this limitation, Dewett and Hensa (2015) combined multiple coherence attributes images using self-organizing maps. Each energy-ratio coherence volume was computed along structure from spectral voices, **u(f):**

$$u(f_l, t_k, x_m, y_m) = a(f_l, t_k, x_m, y_m) \exp[i\varphi(f_l, t_k, x_m, y_m)] \quad (3)$$

constructed using a spectral decomposition algorithm, where **a** is the spectral magnitude and **φ** the spectral phase of each component, *l*. These images were subsequently skeletonized using a commercial swarm intelligence algorithm to provide significantly improved fault images in an Eagle Ford Shale survey.

Sui et al. (2015) also noted the value of multispectral coherence and 3-component limitations of RGB display, and computed coherence based on spectral magnitudes, $a(f_l,t_k,x_m,y_m)$,using the covariance matrix

$$C_{mn} = \sum_{l=1}^{L} \sum_{k=-K}^{K} \left[a(t_k, f_l, x_m, y_m) a(t_k, f_l, x_n, y_n) \right], \quad (4)$$

where L is the number of spectral components. By not using the phase component, the covariance matrix is less sensitive to dip, allowing the use of a simpler, non-structure-oriented computation.

In this presentation, I build on the above work but rather than use the spectral magnitude computed along time slices used in equation 4, I use the spectral voices and their Hilbert transforms computed along structure described by equation 3 to obtain the covariance matrix:

$$C_{mn} = \sum_{l=1}^{L} \sum_{k=-K}^{K} \left[u(t_k, f_l, x_m, y_m) u(t_k, f_l, x_n, y_n) + u^H(t_k, f_l, x_m, y_m) u^H(t_k, f_l, x_n, y_n) \right]. \quad (5)$$

I will then compute coherence from the original broad-band data, from each spectral voice component, and compare them to the multispectral coherence computed using equation 5.

Example 1: Great South Basin, New Zealand

To demonstrate the value of multispectral coherence, let's examine a data volume acquired in the Great South Basin of New Zealand. The left image in Figure 1 shows a time slice at t=1.440 s through "broad-band" energy ratio coherence computing using a 5-trace, 11-sample (±20 ms) through the seismic data after spectral balancing. Block arrows indicate polygonal faulting in the right hand side of the image window and syneresis (commonly called shale dewatering) features in the centre.

I compute seven spectral band-pass filtered data volumes beginning with corner frequencies of 0-10-20-30 Hz and ending with 80-90-100-110 Hz, computing energy ratio coherence for each one. The right image of Figure 1 co-renders three of these coherence images. If all three coherence volumes were perfectly coherent, the corresponding RGB spectral coherence images would add to be white. Areas that appear to be yellow indicate that the higher frequencies are less coherent, areas that that appear to be magenta indicate areas where the mid frequency band is less coherent, while areas that appear to be cyan indicate areas where the low frequency band is less coherent. Areas that appear red indicate that both the mid and the high frequencies are less coherent (leaving the red component). Areas that appear to be green indicate that both the low and the high frequencies are less coherent (leaving the green component). Finally, areas that appear to be black are less coherent for all three frequency filter banks. In this image we note that all three spectral components illuminate the larger faults, such that they appear to be black. The N-S acquisition footprint is strongest at the mid frequencies (magenta), while in the low coherence black "smear" in the broad-band image can now appears as magenta, cyan, or green. In the green area, previously masked syneresis features appear as magenta polygons within a green background.

Figure 2 shows the multispectral coherence computed from all seven filter bank voices defined by the covariance matrix in equation 5. The fault images are much the same as in Figure 1. However, the syneresis features are much better delineated in the multispectral coherence than in the broadband coherence image. Careful examination will show that much of this improvement also is available in the RGB 3-filter-bank image.

Example 2: Fort Worth Basin, Texas, USA

The second example comes from a survey acquired over the Barnett Shale resource play of the Fort Worth Basin of Texas, USA. One of the key objectives of 3D seismic surveys is to identify and avoid geohazards, that either hydraulically connect to an adjoining aquifer, or subtle faults that may result in a horizontal well exiting the target formation. As in the previous example, the data have first been spectrally balanced. The broad band coherence image is shown on the left and the multispectral (seven filter banks) coherence image is shown on the right side of Figure 3. There is only a slight improvement in the fault delineation in the NW part of the survey; however, karst features previously masked by a broad incoherent zone now appear as discrete, low coherence anomalies; implying that they are incoherent at all frequencies. Two subtle channels also appear.

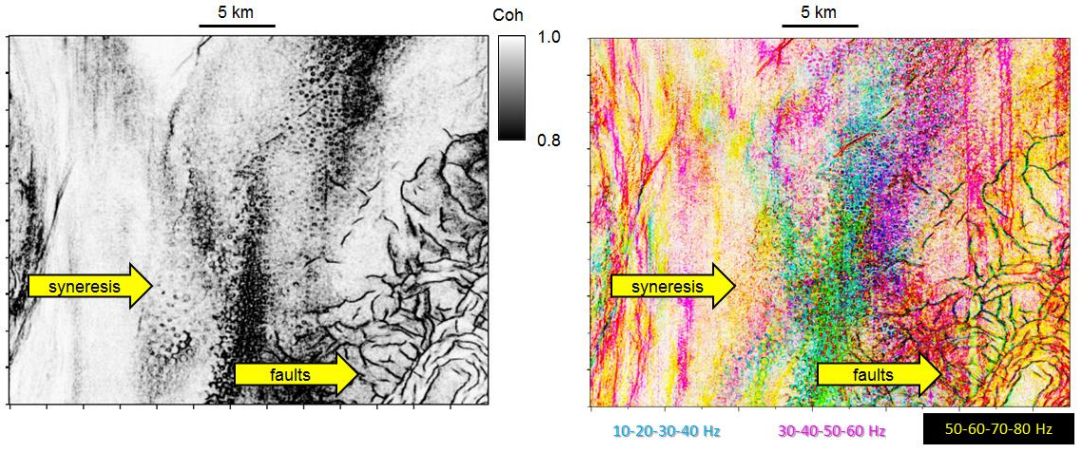

Figure 1 *Time slices at t=1.44 s through (Left) "Broad-band" coherence computed from the seismic amplitude data after spectral balancing, and (Right) co-rendered coherence for three of the spectral bands.*

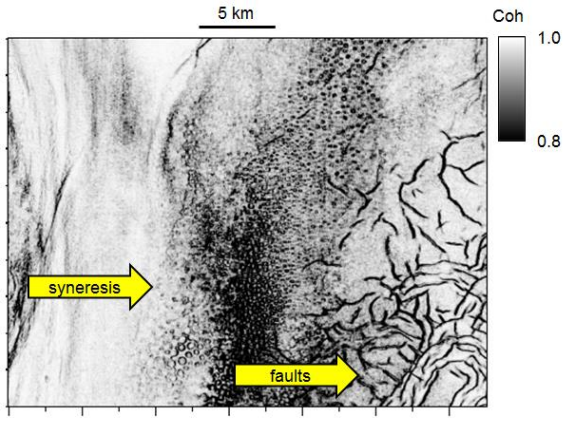

Figure 2 *The same time slice as shown in Figure 1, but now through multispectral coherence computed using all seven spectral bands. The larger faults appear much the same, though there is less background blur for the multispectral coherence. The resolution of the syneresis features is significantly improved over the broadband coherence image, although the detailed information content is similar to that in the co-rendered three-filter-bank RGB image of Figure 1.*

Conclusions

Multispectral coherence provides improved images over traditional coherence images, even if the seismic amplitude data have been previously spectrally balanced. While much of this improvement can also be found in RGB blended volumes, multispectral coherence provides several advantages: (1) one can combine the information content of more than three coherence volumes, (2) there is only one rather than three volumes to be loaded into the workstation, which may be a limitation for very large

data sets, and (3) the grey-scale image shown in Figure 2 can be co-rendered with other attributes of interest plotted against a polychromatic colour bar, such as P-impedance vs. Poisson's ratio or SOM cluster results. Although the computation cost increases with the number of filter banks, the added time savings in interpreting ambiguous faults and the revelation of previously hidden features is of significant value to the human interpreter.

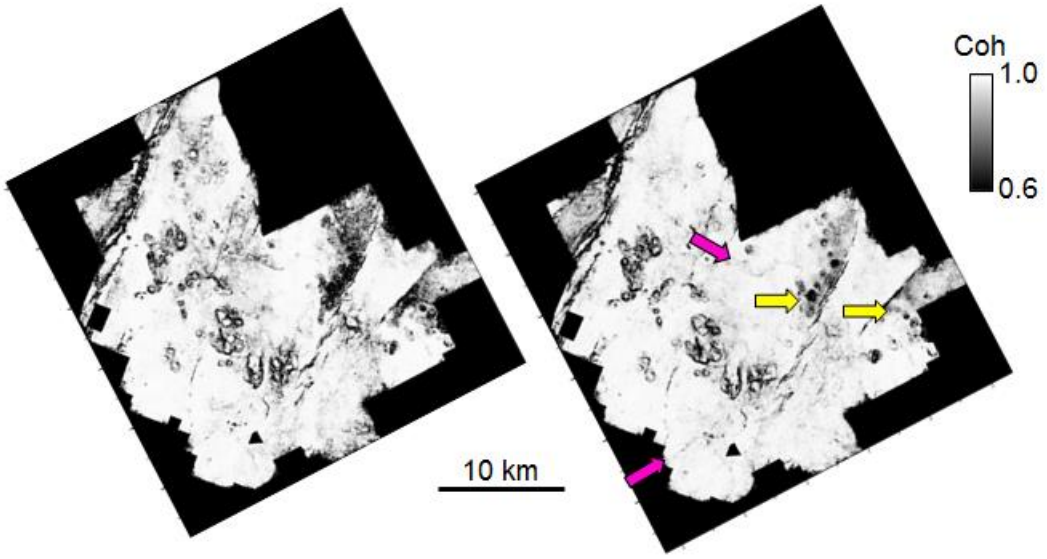

Figure 3 *Time slice at t=0.7 s through coherence computed from (Left) the original broad band data, and (Right) seven spectral bands at the Barnett Shale interval. Arrows indicate improvement in delineation of channels (magenta) and karst collapse (yellow). (Data courtesy of Marathon Oil Co.)*

Acknowledgements

Thanks to the industry sponsors of the University of Oklahoma Attribute-Assisted Seismic Processing and Interpretation consortium for their technical guidance and financial support. Thanks also to the New Zealand Petroleum Ministry for providing a volume of their GSB survey and to Marathon Oil Co. for their Fort Worth Basin survey for use in this study.

References

Chopra, S., and Marfurt, K. J. [2007] Seismic attributes for prospect identification and reservoir characterization. SEG Geophysical Development Series, 11.

Dewett, D. T, and Hensa, A. A. [2015] Spectral similarity fault enhancement. *Interpretation*, 4, SB149-SB159.

Gao, D. [2013] Wavelet spectral probe for seismic structure interpretation and fracture characterization: A workflow with case studies. *Geophysics*, 78, O56-O67.

Gersztenkorn, A., and Marfurt, K. J. [1999] Eigenstructure-based coherence computation as an aid to 3-D structural and stratigraphic mapping. *Geophysics*, 64, 1468-1479.

Hardage, B. [2009] Frequencies are fault finding factors: Looking low aids data interpretation. *AAPG Explorer, 30, no 9, 34.*

Honorio, B. C. Z., Correia, U. M. da C., Matos, M. C. de, and Vidal, A. C. [2016] Similarity attributes from differential resolution components. *Interpretation*, 4, T65-T73.

Li, F., and Lu, W. [2014] Coherence attribute at different spectral scales. *Interpretation*, 2, 1-8.

Sui, J.-K., Zheng, X.-D. and Li, Y.-D. [2015] A seismic coherency method using spectral attributes. *Applied Geophysics*, 12, no. 3, 353-361.